Downloaded from orbit.dtu.dk on: Apr 25, 2024

DTU Library

Buckling and yield strength estimation of architected materials under arbitrary loads

Andersen, Morten N.; Wang, Yiqiang; Wang, Fengwen; Sigmund, Ole

Published in:
International Journal of Solids and Structures

Link to article, DOI:
10.1016/j.ijsolstr.2022.111842

Publication date:
2022

Document Version
Publisher's PDF, also known as Version of record

Link back to DTU Orbit

Citation (APA):
Andersen, M. N., Wang, Y., Wang, F., & Sigmund, O. (2022). Buckling and yield strength estimation of architected materials under arbitrary loads. *International Journal of Solids and Structures*, *254-255*, Article 111842. https://doi.org/10.1016/j.ijsolstr.2022.111842

General rights
Copyright and moral rights for the publications made accessible in the public portal are retained by the authors and/or other copyright owners and it is a condition of accessing publications that users recognise and abide by the legal requirements associated with these rights.

- Users may download and print one copy of any publication from the public portal for the purpose of private study or research.
- You may not further distribute the material or use it for any profit-making activity or commercial gain
- You may freely distribute the URL identifying the publication in the public portal

If you believe that this document breaches copyright please contact us providing details, and we will remove access to the work immediately and investigate your claim.

International Journal of Solids and Structures 254–255 (2022) 111842

Contents lists available at ScienceDirect

International Journal of Solids and Structures

journal homepage: www.elsevier.com/locate/ijsolstr

Buckling and yield strength estimation of architected materials under arbitrary loads

Morten N. Andersen [a], Yiqiang Wang [b], Fengwen Wang [a], Ole Sigmund [a,*]

[a] Department of Civil and Mechanical Engineering, Solid Mechanics, Technical University of Denmark, DK-2800, Lyngby, Denmark
[b] State Key Laboratory of Structural Analysis for Industrial Equipment, Dalian University of Technology, 116024, China

ARTICLE INFO

Keywords:
Microstructural buckling
Buckling strength surfaces
Yield strength surfaces
Architected materials

ABSTRACT

Buckling strength estimation of architected materials has mainly been restricted to load cases oriented along symmetry axes. However, realistic load scenarios usually exhibit more general stress distributions. This study employs local member analyses to estimate the buckling strength surface of stretch-dominated lattice structures. As an integral part of the method, the yield strength surface is also determined. Local members are analyzed under different boundary conditions, i.e., simply-supported, clamped as well as rotational springs accounting for lattice topologies. The local member estimations are compared with accurate but expensive numerical linear microstructural buckling analyses for different loadings. The local member approach provides a valuable tool to quickly estimate the microstructural buckling strength of stretch-dominated lattice structures, especially for applications where the stress state is non-uniform such as infill in additive manufacturing. Using the local member approach, we compute the entire buckling strength surfaces of an orthotropic bulk modulus optimal plate, an isotropic stiffness optimal plate, and an isotropic truss lattice structure subjected to rotated uni-axial loads. All the considered lattice structures possess high buckling strength anisotropy. In addition, the isotropic stiffness optimal plate structure possesses a near-isotropic yield strength surface while the truss counterpart possesses an anisotropic one. Inspired by the buckling strength surface calculations, we further propose a new isotropic plate lattice configuration with enhanced buckling strength isotropy without stiffness or yield strength deterioration.

1. Introduction

Architected materials with ultimate stiffness and strength are pushing the limits for high performance light-weight structures. In particular, exploiting architected materials as infill for additive manufacturing has shown to vastly increase macroscopic buckling strength while decreasing stiffness very little compared to equal volume solid counterparts. For instance, Clausen et al. (2016) obtained over 400% buckling strength improvement, while only losing 20% in stiffness for a particular optimized beam structure. However, with ever increasing demands for light-weight, optimized structures and advances in manufacturing techniques, plate and truss microstructures are realizable with lower volume fractions and higher slenderness, which make them prone to local buckling failure and therefore necessitate efficient microscopic instability analysis.

It has been shown that the onset of failure of honeycombs is extremely sensitive to load orientation and ratios of principal macroscopic stresses (Triantafyllidis and Schraad, 1998). Detailed knowledge of yield and buckling strength performance of architected materials under arbitrary loading is thus essential for their applications in complex structures subjected to various loading scenarios. Therefore, in this paper, we focus on investigating yield and buckling strength surfaces for several architected materials under arbitrary directional loadings.

Previously, many studies have been devoted to investigate microstructural buckling strength for prescribed loadings, where both simplified approaches and refined numerical approaches have been employed. A simplified approach is to analyze the buckling strength of individual plate or truss/beam members, where the geometry and boundary conditions are approximated by known analytical solutions (Christensen, 1986; Valdevit et al., 2013; Latture et al., 2018; Tancogne-Dejean and Mohr, 2018; Haghpanah et al., 2014). However, Deshpande et al. (2001) concluded that the simply-supported boundary conditions may only provide lower bounds on the buckling strength of the overall microstructure, while the clamped boundary conditions may similarly provide upper bounds. Microstructural buckling of both random and periodic porous elastomers under large deformations was investigated by using numerical methods (Triantafyllidis et al., 2006; Michel et al.,

* Corresponding author.
E-mail address: olsi@dtu.dk (O. Sigmund).

https://doi.org/10.1016/j.ijsolstr.2022.111842
Received 27 January 2022; Received in revised form 31 May 2022; Accepted 5 July 2022
Available online 28 July 2022
0020-7683/© 2022 The Authors. Published by Elsevier Ltd. This is an open access article under the CC BY license (http://creativecommons.org/licenses/by/4.0/).

2007). In 3D, the macroscopic buckling failure of random porous elastomers was investigated and detected by loss of strong ellipticity in the homogenized constitutive matrix, using second-order homogenization theory that assumes linear comparison composites (Lopez-Pamies and Castañeda, 2007a,b). These macroscopic instabilities were also experimentally observed for 3D honeycombs under uni-axial and bi-axial loading (Papka and Kyriakides, 1994, 1999). In addition, macroscopic instability of honeycombs under dynamic loading was investigated in Bordiga et al. (2021). Recently, an accurate and systematic study on microstructural buckling strength under static loading was performed for several 3D lattice structures, using expensive FE analysis combined with Floquet–Bloch wave theory to determine the critical buckling strength considering both local and global buckling under uni-axial compressions (Andersen et al., 2020). A subsequent study (Wang and Sigmund, 2021) employed topology optimization methods to design 3D microstructures with significantly enhanced buckling strength under uni-axial compression.

The simplified approach is based on crude assumptions and does not account for lattice topologies, resulting in significant estimation errors. On the other hand, the more sophisticated numerical models provide high accuracy but require significantly more development efforts and computational cost. Furthermore, previous instability studies have mainly focused on well-defined load cases along principal axes. To the best of the authors' knowledge, no investigation has been carried out on providing complete directional buckling strength surfaces of 3D architected materials due to the associated computational cost. However, the response of 3D architected materials under arbitrary loads regarding stiffness and strength is essential for practical applications and therefore deserves further investigation.

Inspired by the simplified approach, this study employs local member analyses to estimate the buckling strength of plate and truss lattices. Besides simply-supported and clamped boundary conditions and their average, rotational spring boundary conditions are investigated for their ability to improve estimation accuracy, extending the rotational spring boundary conditions in Gibson et al. (1982) to 3D, where 2D cellular materials were studied for their buckling strength using column buckling with a rotational spring at each end. The different boundary conditions are validated using sophisticated linear microstructural buckling analyses (Andersen et al., 2020), which has been shown to provide good predictions compared to nonlinear post-buckling studies and experimental results (Wang and Sigmund, 2020a; Bluhm et al., 2022; Wang et al., 2022). We apply this approach to study the uni-axial buckling strength of stretch-dominated lattice structures as a function of the load direction, but the approach is general and valid for arbitrary loads. As representatives of different types of stretch-dominated lattice structures, we study a class of stiffness-optimal microstructures from the literature (Berger et al., 2017; Gurtner and Durand, 2014), i.e., an orthotropic simple-cubic plate lattice structure (SC-PLS), an isotropic plate lattice structure (Iso-PLS), and an isotropic truss lattice structure (Iso-TLS) shown in Fig. 1. Specifically, these isotropic lattice structures are combinations of simple cubic (SC) and body-centered cubic (BCC) members. While the PLSs offer superior stiffness and yield strength, the microstructural yield and buckling strength surfaces can be vastly different. In contrast, the TLS strength surfaces are very similar for both yield and buckling failure, in turn resulting in more predictable failure mechanisms purely based on volume fractions. Based on the knowledge and results obtained, we propose a new near-optimal Iso-PLS with an improved isotropic buckling strength surface, with no deterioration of the stiffness and yield strength.

The paper is organized as follows. Section 2 first briefly summarizes linear microstructural buckling strength analysis and then presents the local member approach and corresponding validations. Section 3 employs it to study the buckling strength of the investigated lattice structures under rotating uni-axial loads and the yield surface with further verification with linear microstructural buckling analysis. Moreover, a new microstructure is proposed with enhanced buckling strength isotropy. Finally, conclusions are drawn in Section 4.

2. Methods

Buckling modes of lattice structures can be local, global, or in-between (Andersen et al., 2020), where triggering of each mode type depends on the local stress state in the members and their connectivity. Local modes are characterized as periodic or anti-periodic cell-wise buckling modes, i.e. the periodicity of the buckling mode spans one or two unit cells. Global modes are characterized by the periodicity of buckling modes being much larger than the size of the unit cell. Although deeper investigations are needed to definitively determine what trigger(s) the global modes, a general promoter of global (shear) modes is related to low shear stiffness, which is seen from the band diagram presented in Fig. 2 of Andersen et al. (2020). Compared to the fact that the local mode lattice structures SC-PLS, Iso-PLS and Iso-TLS have Zener anisotropy ratios of 0.45, 1.00 and 1.00, respectively, the SC-TLS suffering from the global buckling mode has a small Zener anisotropy ratio of 0.12. Assuming sufficient shear stiffness, buckling instabilities in stretch-dominated lattice structures are thus predominantly governed by cell-local modes. That is, the plate and truss/beam components buckle in repeated periodic or anti-periodic cell-wise patterns. Hence, it is possible to estimate the microstructural buckling strength by performing analysis on an individual plate or beam member, where the lowest buckling strength among all the members determines the effective buckling strength of the lattice structure.

In the following section, we first briefly summarize the linear microstructural buckling analysis in Andersen et al. (2020) and then focus on the local member approach with local member buckling analysis and corresponding validations.

2.1. Numerical microstructural buckling analysis

The microstructural buckling strength of a lattice structure subjected to a global stress state $\boldsymbol{\sigma}^0 = \left[\sigma_1, \sigma_2, \sigma_3, \sigma_4, \sigma_5, \sigma_6\right]^T$ is calculated by using finite element-based linear microstructural buckling analysis. First, the homogenized elasticity matrix, $\boldsymbol{D}^H$, is calculated using a computational homogenization method (Guedes and Kikuchi, 1990; Sigmund, 1994; Bensoussan et al., 2011). Then the global stress state $\boldsymbol{\sigma}^0$ is converted to a local pre-stress $\boldsymbol{\sigma}_e^0$ in a given finite element e via a global strain $\boldsymbol{\varepsilon}^0$, stated as

$$\boldsymbol{\sigma}_e^0 = \boldsymbol{D}_e \boldsymbol{\varepsilon}^0 = \boldsymbol{D}_e \left(\boldsymbol{D}^H\right)^{-1} \boldsymbol{\sigma}^0, \tag{1}$$

where $\boldsymbol{D}_e$ is the elasticity matrix of the solid constituent. The real stress state $\boldsymbol{\sigma}$ in the microstructure is obtained under periodic boundary conditions subjected to the pre-stress stated in Eq. (1). Now multiple linear buckling analyses are performed to calculate the microstructural buckling strength, where instabilities of the short- and long wavelength are captured by employing Floquet–Bloch boundary conditions (Triantafyllidis and Schnaidt, 1993; Neves et al., 2002; Thomsen et al., 2018; Andersen et al., 2020), given as

$$\begin{aligned} &\left[\boldsymbol{K}_0 + \lambda \boldsymbol{K}_s(\boldsymbol{\sigma})\right] \boldsymbol{\Phi} = \boldsymbol{0} \\ &\boldsymbol{\Phi}|_{x=\Gamma_{\text{Front}}} = e^{ik_1} \boldsymbol{\Phi}|_{x=\Gamma_{\text{Back}}}, \quad \boldsymbol{\Phi}|_{y=\Gamma_{\text{Right}}} = e^{ik_2} \boldsymbol{\Phi}|_{y=\Gamma_{\text{Left}}}, \\ &\boldsymbol{\Phi}|_{z=\Gamma_{\text{Top}}} = e^{ik_3} \boldsymbol{\Phi}|_{z=\Gamma_{\text{Bottom}}}. \end{aligned} \tag{2}$$

Here the unit cell has unit size, $\boldsymbol{K}_0$ is the initial stiffness matrix, $\boldsymbol{K}_s(\boldsymbol{\sigma})$ is the stress stiffness matrix depending on the macroscopic load and λ is the eigenvalue with the associated eigenvector $\boldsymbol{\Phi}$ that is subjected to the Floquet–Bloch boundary conditions, $i = \sqrt{-1}$ is the imaginary unit, $\Gamma_{\square}$ denotes faces of the unit cell and $\boldsymbol{k} = \left[k_1, k_2, k_3\right]^T$ is the wavevector to capture all possible buckling modes. The microstructural buckling strength is defined as $\sigma_c = \lambda_{\min} \|\boldsymbol{\sigma}^0\|$, where $\|\cdot\|$ represents the 2-norm and $\lambda_{\min}$ is the lowest eigenvalue over all wavevectors $\boldsymbol{k}$ swept along the irreducible Brillouin zone edges. The irreducible Brillouin zone is determined by shared symmetries in the geometry and loading (Andersen et al., 2020). However, for complex load cases without load symmetries, the required sweep becomes significantly

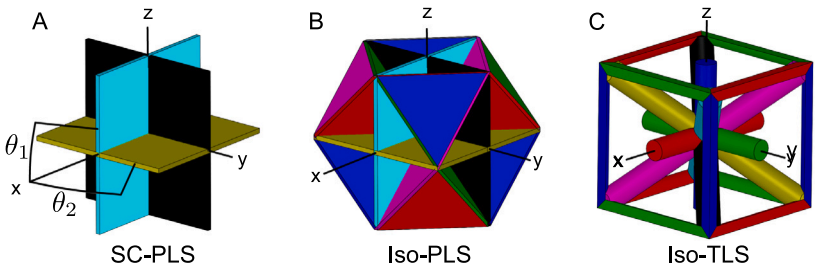

Fig. 1. Investigated lattice structures. A: Simple cubic plate lattice structure (SC-PLS). B: Simple cubic+body centered cubic isotropic plate lattice structure (Iso-PLS). C: Simple cubic+body-centered cubic isotropic truss lattice structure (Iso-TLS). The members are color coded where members with the same color have the same orientation and therefore constitute a member set.

larger and may cover the entire Brillouin zone. Even for load cases that can be reduced to the edges of the irreducible Brillouin zone, a large number of 3D linear buckling analyses (Eq. (2)) is required to accurately determine the microstructural buckling strength. This results in CPU times up to 100 hours on a supercomputer as discussed at the end of Section 3. Hence, cheaper buckling strength estimation methods are needed to systematically investigate the microstructural buckling strength under arbitrary loads.

2.2. Local member approach

Linear microstructural buckling strength analysis in Andersen et al. (2020) showed that the critical buckling modes of stretch-dominated microstructures with sufficient shear stiffness are determined by local member buckling. Hence, the effective buckling strength of microstructures can be estimated based on the buckling strength of local members. In this section, we present a local member approach to estimate material buckling strength. The local members can be analyzed subjected to different boundary conditions, such as simply-supported and clamped conditions in the analytical calculations (Christensen, 1986; Valdevit et al., 2013; Latture et al., 2018; Tancogne-Dejean and Mohr, 2018; Deshpande et al., 2001). To account for the lattice topologies, we also present a rotational spring boundary case. For the rotational spring boundary condition, the adjacent members that provide rotational stiffness are approximated and converted to bending moments that provide rotational stiffness and reduce the geometric complexity.

2.2.1. Stress calculation in local members

The global stress $\boldsymbol{\sigma}^0$ is converted to the local stress state in each beam or plate member using the homogenized elasticity matrix $\boldsymbol{D}^H$. In this paper, the homogenized elasticity matrix for volume fraction $f < 10^{-2}$ is calculated using a semi-analytical add-up model (Christensen, 1986; Bourdin and Kohn, 2008), whereas numerical homogenization and finite element analyses are used at higher volume fractions up to $f \approx 0.5$ (Guedes and Kikuchi, 1990; Sigmund, 1994; Bensoussan et al., 2011). As in Eq. (1), the global stress is first converted to a global strain via

$$\boldsymbol{\varepsilon}^0 = \left(\boldsymbol{D}^H\right)^{-1} \boldsymbol{\sigma}^0. \tag{3}$$

The global strain (converted to a matrix as indicated by the subscript m) is then projected to each local member coordinate system using

$$\boldsymbol{\varepsilon}'_{\mathrm{m}} = \mathbf{T}\boldsymbol{\varepsilon}^0_{\mathrm{m}}\mathbf{T}^T \tag{4}$$

where $\mathbf{T}$ is a rotation matrix describing the local member coordinate system. Finally, the projected strain is converted to a local member pre-stress by

$$\boldsymbol{\sigma}^0_{\mathrm{loc}} = \boldsymbol{D}_{\mathrm{loc}}\boldsymbol{\varepsilon}' \tag{5}$$

where $\boldsymbol{D}_{\mathrm{loc}}$ is the local elasticity matrix. The actual stresses $\boldsymbol{\sigma}$ in the local member are obtained by solving the local member stationary equilibrium under the considered boundary conditions.

Eq. (5) refers to the stress that is applied to beam or plate elements. Only the in-plane/axial stress components are considered for plates/beams in the local member approach. Specifically, for the plate case, the considered planar stresses are σ_{11}, $\sigma_{12} = \sigma_{21}$ and σ_{22}. For the beam case, only the axial stress σ_{11} is considered. This is a reasonable assumption due to the stretch-dominated microstructures considered and the use of linear buckling theory. As in the accurate numerical microstructural evaluation in Section 2.1, the above mentioned stress is applied to the local member as external stress. Note that we neglect the contributions from intersections, hence parallel members in one group (see the colored members in Fig. 1) are subjected to identical local stresses. This stress approximation approach is found to be sufficiently accurate and used here for moderate volume fractions up to 0.3, based on comparisons with accurate 3D finite element analyses.

In the following, we use unit Young's modulus $E_0 = 1$ with Poisson's ratio $\nu_0 = 1/3$ for the base constituent. Due to linearity, physical values of stiffness and strength estimates can simply be obtained by multiplication with the physical Young's modulus. Based on the stress calculation, the microstructural yield strength is calculated as

$$\sigma_y = \bar{\sigma}_y \sigma_0 = \frac{\|\boldsymbol{\sigma}^0\|}{\sigma_{\mathrm{vm,max}}}\sigma_0 \tag{6}$$

where $\sigma_{\mathrm{vm,max}}$ is the maximum von Mises stress of all members under the given load case, σ_0 is the yield strength of the base material and $\bar{\sigma}_y$ denotes the relative yield strength. This relative yield strength (like many other material properties) is commonly seen in the literature as σ_y/σ_0 (Valdevit et al., 2013; Berger et al., 2017; Tancogne-Dejean et al., 2018) . The 2-norm of the load enables comparison between different load magnitudes and scenarios. Utilizing relative strength properties is beneficial as different base materials can be inserted into Eq. (6).

2.2.2. Local member buckling analysis

The simplest microstructural buckling strength estimations consist of approximating the beam and plate members as known analytical solutions, i.e., simple column or plate buckling with simply-supported (Fig. 2A) or clamped (Fig. 2B) boundary conditions (Christensen, 1986; Valdevit et al., 2013; Latture et al., 2018; Tancogne-Dejean and Mohr, 2018; Haghpanah et al., 2014). However, as individual plate or truss/beam members are connected to varying numbers of adjacent members that provide rotational stiffness, neither simply-supported nor clamped boundary conditions are appropriate but may only be used as lower or upper bounds. As an alternative, we investigate a simple and flexible boundary condition, i.e., rotational spring boundaries (Fig. 2C), where the adjacent members determine the rotational stiffness. Several approaches may be envisioned to account for adjacent members, but the proposed approach comprises applying simple supports with the addition of rotational springs to the boundaries/ends to approximate the rotational stiffness contributions from neighboring members. Herein, the spring stiffness of adjacent members for both plates and trusses is approximated by beam theory, where beam stiffeners are distributed along the edge (see Fig. 2) for the plate case. The critical buckling modes of plates and beams are assumed to

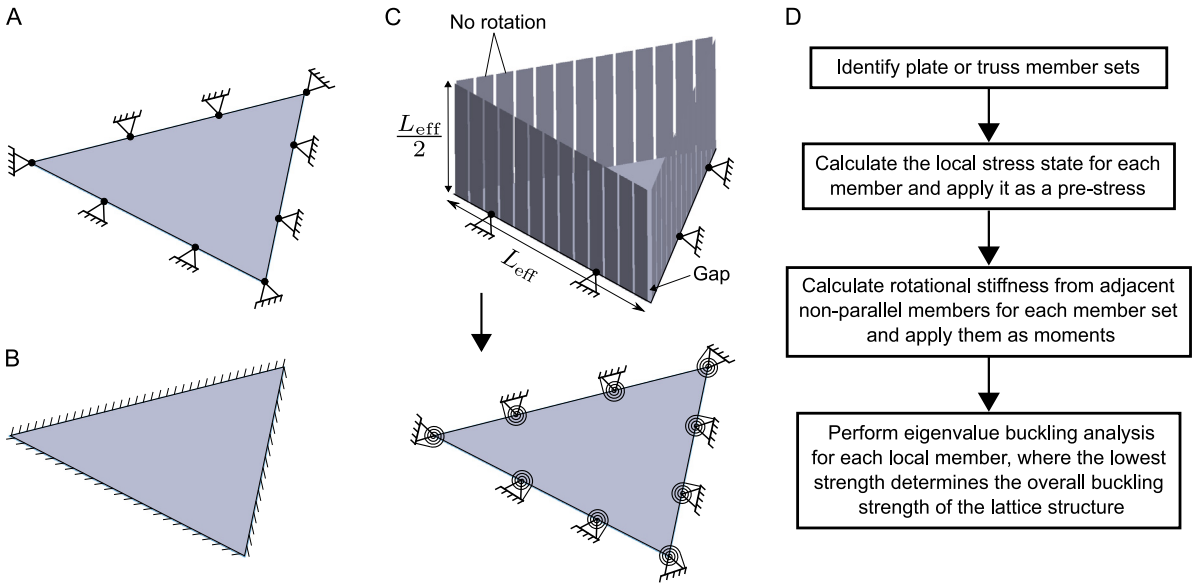

Fig. 2. Illustration of different boundary conditions in the local member approach based on a BCC triangle plate in Iso-PLS. A: Simply-supported. B: Clamped. C: Equivalent rotation springs. Top: Plate with one set of adjacent wall stiffeners. The edges of the base plate have simply supported boundary conditions, while the top edges of the wall stiffeners have no rotation allowed and hence mimic a distributed cantilever beams with end moments. Bottom: Equivalent rotational spring boundary conditions. D: Flow chart for the local member approach.

deform in half-sine waves (based on extensive numerical observations). Therefore, the springs are approximated by the stiffness of a cantilever beam subjected to an end moment, as it resembles a quarter sine wave. The rotational stiffness, denoted by k_t, can thus be applied as a moment that acts in the opposite direction of the buckling deformation and stiffens the boundaries. The boundary moment M is defined as

$$M = k_t \phi \tag{7}$$

where ϕ is the rotation angle around plate edges or beam ends. This equation has the same form as a cantilever beam subjected to an end moment, which is

$$M = \frac{E_0 I}{(L_{\text{eff}}/2)} \phi. \tag{8}$$

Here I is the second moment of area of the adjacent stiffener with $\nu_0 = 0$ allowing for analytical expression and treating plates as wide beams, L_{eff} is the effective length defined as $L_{\text{eff}} = L - t/2$, where L and t are the member length and thickness, respectively. The effective length is used to account for shortening effects from intersecting members. Due to the overlap and interaction between crossing bars/plates, $L_{\text{eff}} = L$ would overestimate and $L_{\text{eff}} = L - t$ would underestimate the true length. Based on extensive numerical experiments, we find that $L_{\text{eff}} = L - t/2$ provides the best estimated value. This assumption is grossly simplified but is used here for the sake of simplicity and keeping identical assumptions for both types of lattice structures. Furthermore, adjacent parallel members do not add rotational stiffness as they are subjected to the same local stress and therefore buckle in a continuous wave. Consequently, the rotational stiffness of a non-parallel adjacent stiffener is split between the connected parallel members. The resulting moment summed up from adjacent members is

$$M = \sum_{n=1}^{N} \left(\frac{\frac{E_0 I_n}{(L_{\text{eff},n}/2)}}{2} \right) \phi = \sum_{n=1}^{N} \left(\frac{E_0 I_n}{L_{\text{eff},n}} \right) \phi \tag{9}$$

where N indicates the number of adjacent non-parallel members.

Based on Timoshenko beams or Mindlin plates with quadratic finite elements, linear buckling analysis is performed to determine the buckling strength of the j'th member, given as

$$\left[\boldsymbol{K}_0^j + \lambda_1^j \boldsymbol{K}_s^j(\boldsymbol{\sigma}) \right] \boldsymbol{\Phi}_1^j = \boldsymbol{0}, \tag{10}$$

where λ_1^j and $\boldsymbol{\Phi}_1^j$ are the fundamental eigenvalue and associated buckling mode of the j'th member. The microstructural buckling strength is determined by the minimum eigenvalue among all the members, given as

$$\sigma_c = \left(\min_j \lambda_1^j \right) \|\boldsymbol{\sigma}^0\|. \tag{11}$$

The relative buckling strength is then $\tilde{\sigma}_c = \sigma_c / E_0$. Obviously, this planar FE analysis is significantly cheaper than a full 3D microstructures buckling analysis considering all possible wave-vector in the Floquet–Bloch boundary conditions.

The flow chart of the local member approach is presented in Fig. 2D. It is summarized in four steps:

1. Identify plate or truss member sets (Fig. 1).
2. Calculate the local stress for each member set and apply it as pre-stress (Eqs. (3)–(5)).
3. Set up boundary conditions for the local member buckling analysis, i.e., simply-supported, clamped, and rotational springs described in Eq. (9).
4. Perform linear buckling analysis for each member set. The lowest eigenvalue determines the effective buckling strength of the microstructures (Eqs. (10)–(11)).

For 2D and 3D truss microstructures, it is rather trivial to exchange neighbor elements with rotational springs, however, for plate microstructures, adding accurate rotational stiffness substituting neighbor plate element stiffnesses would require advanced and expensive analysis, defying the purpose of the simplified model. Anyway, the neighboring plates have different dimensions and shapes and hence accurate modeling of their contributions is impractical. Therefore, we resort to the simple rotational spring model that physically can be interpreted as the illustrated model. The suggested distributed moment boundary conditions are expected to provide a lower bound to the true strength that is more accurate than simple supports.

2.3. Validation

In this subsection, we illustrate and verify the rotational spring boundaries using buckling analysis of a beam and plate member with

Table 1
Comparison of member stiffeners versus rotational springs exerted as moments.

Case	Rotational springs	Member stiffeners	Error %
Iso-TLS: 1 stiffener (Fig. 3A)	9.928E-4	9.928E-4	0
Iso-TLS: 2 stiffeners (Fig. 3B)	1.196E-3	1.196E-3	0
SC-PLS: 1 set stiffeners (Fig. 4A)	2.613E-3	2.616E-3	0.11
SC-PLS: 2 set stiffeners (Fig. 4B)	2.939E-3	2.945E-3	0.20

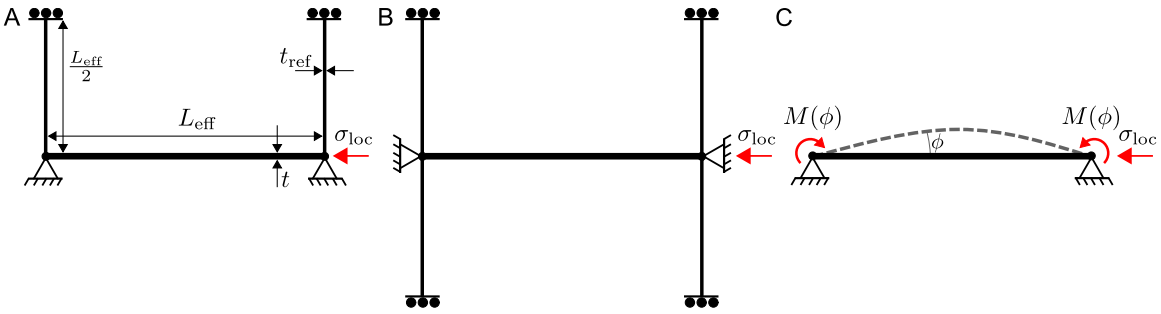

Fig. 3. A truss example. The base truss is the thick horizontal truss, which is simply-supported at the ends. The thinner vertical bars are beam stiffeners that have no rotation allowed at the opposite ends of the base truss ends. A: Base truss with one beam stiffener at each end. B: Base truss with two beam stiffeners at each end. C: The corresponding rotational spring boundaries where the rotational stiffness from adjacent beam stiffeners has been converted to moments.

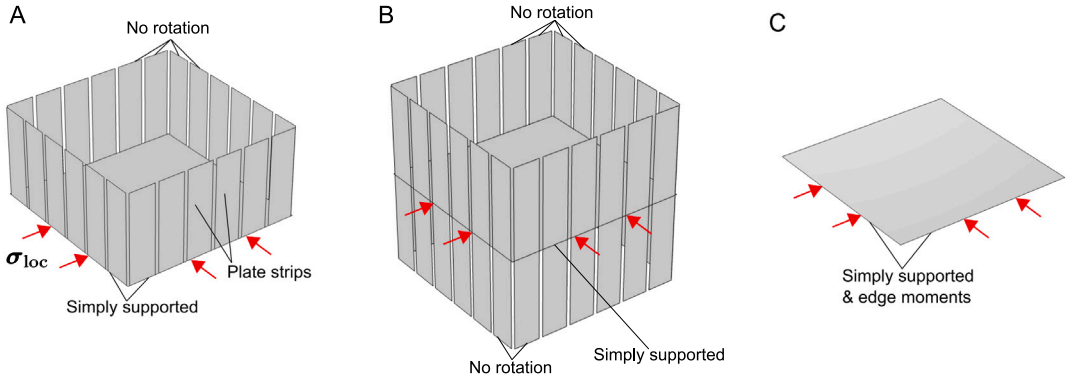

Fig. 4. A plate example. The base plate is the horizontal plate, which is simply-supported at the edges. The vertical wall stiffeners have no rotation allowed at the opposite edges of the base plate edges. A: Base plate with one set of wall stiffeners per edge. B: Base plate with two set of wall stiffeners per edge. C: The corresponding simplified model where the rotational stiffness from adjacent wall stiffeners has been converted to moments (analogous to Fig. 3C).

stiffeners (Figs. 3 and 4). Then, the local member approaches subjected to different boundary conditions are compared by estimating the microstructural buckling strength versus volume fractions of the investigated lattice structures subjected to a uni-axial load (Fig. 5).

2.3.1. Member buckling

A truss and a plate example with stiffeners are considered to illustrate and verify the rotational spring boundaries. Specifically, one and two stiffeners per beam end or plate edge are compared to the corresponding model, where the rotational stiffness from adjacent stiffeners is converted to moments. The truss example is shown in Fig. 3, while the plate example is analogous and shown in Fig. 4. The applied load is aligned with the Cartesian x-axis (see Fig. 1).

The truss example is a simplification of the red SC truss of the Iso-TLS (see Fig. 1C), but only stiffened by one or two beam per end. The truss length and thickness are $L = 1$ and $t = 0.144$, respectively, resulting in an effective length $L_{\text{eff}} = L - t/2 = 0.928$. The reference thickness t_{ref} of the adjacent stiffener that provides half rotational stiffness to the base SC truss, is calculated from $I(t)/2 = I(t_{\text{ref}})$ resulting in $t_{\text{ref}} = t/\sqrt[4]{2}$. Furthermore, the applied axial stress to the base truss is $\sigma_{\text{loc}} = -19.292$. Fig. 3A and B show the base truss with one and two beam stiffeners per end, respectively. Fig. 3C shows the corresponding rotational spring boundaries where the adjacent beam stiffeners have been converted to end moments proportional to the end rotation ϕ. The resulting buckling strengths are shown in Table 1. The results from beam stiffeners and rotational springs are identical for both one and two adjacent stiffeners. This confirms that the simplification proposed here is effective.

The plate example is based on the yellow plate of the SC-PLS (see Fig. 1A). The plate side length and thickness are $L = 1$ and $t = 0.0717$, respectively, resulting in an effective length of $L_{\text{eff}} = L - t/2 = 0.964$. The reference thickness t_{ref} of the adjacent stiffener that yields half rotational stiffness to the base plate, is calculated from $I(t)/2 = I(t_{\text{ref}})$ resulting in $t_{\text{ref}} = t/\sqrt[3]{2}$. Furthermore, the planar stress applied to the base plate is $\sigma_{\text{loc}} = [-7.168, -1, 230, 0]^T$. Figs. 4 A and B show the base plate with one and two wall stiffeners per edge, respectively. Fig. 4C shows the corresponding local member approach with rotational spring boundaries where the adjacent wall stiffeners have been converted to edge moments. The resulting buckling strengths are also shown in Table 1. The results from the beam stiffeners and rotational springs show minor deviations for both one and two set adjacent stiffeners, hence, confirm that the simplification proposed here is effective.

In summary, the rotational spring boundaries can efficiently account for the stiffening effects from adjacent members by converting rotational stiffness from adjacent members into moments.

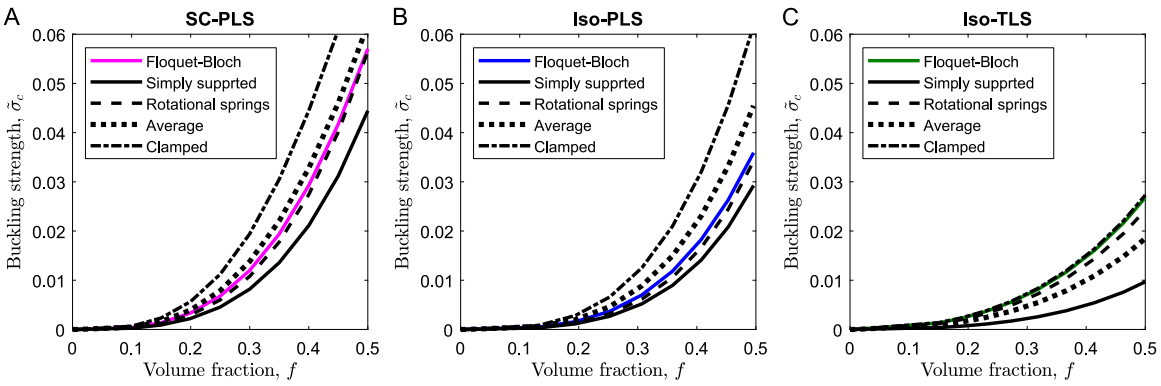

Fig. 5. Relative buckling strength versus volume fraction for the uni-axial case of the load aligned with a principal axis, i.e., the Cartesian x-axis (see Fig. 1). Simply-supported, rotational springs and clamped boundary conditions are compared to full Floquet–Bloch results. A: SC-PLS. B: Iso-PLS. C: Iso-TLS.

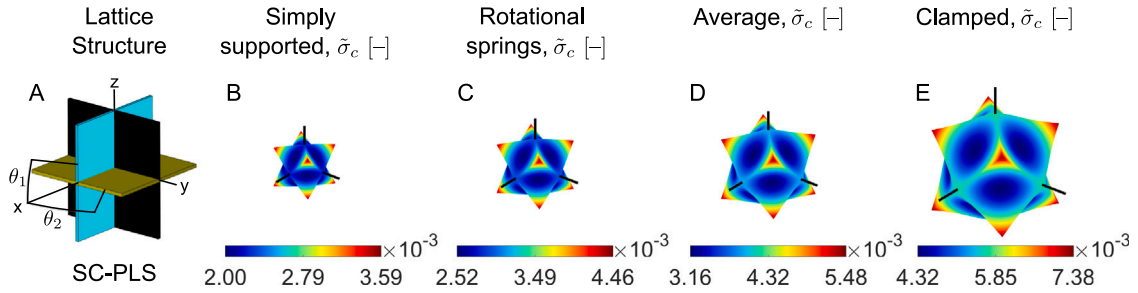

Fig. 6. Relative buckling strength surfaces of SC-PLS subjected to different boundary conditions. A: Lattice typology with colored plate member sets and depiction of load orientation described by two Euler angles. B-E: Buckling strength surface from applying different boundary conditions. B: Simply-supported boundary conditions. C: Rotational springs. D: The average result of the simply-supported and clamped boundary conditions. E: Clamped boundary conditions. All surfaces are depicted with Cartesian coordinate system axes.

2.3.2. *Microstructural buckling strength estimation*

To investigate the performance of the spring model compared to the "exact" Floquet–Bloch and other simplified models (Fig. 2), the microstructural buckling strength is determined for the considered lattice structures under uni-axial loading (see Fig. 1).

Fig. 5 shows the buckling strength estimation under an uni-axial load along the x-axis using the local member approaches with simply-supported (solid lines), rotational spring (dashed lines), and clamped boundary conditions (dash-dotted line). In addition, the averaged buckling strength estimation of the simply-supported and clamped cases is also provided, denoted by dotted lines. These results are compared to the true buckling strength analysis using Floquet–Bloch theory in Section 2.1. For SC-PLS and Iso-PLS, it is clearly seen that the simply-supported and clamped boundary conditions significantly under- and over-estimate the buckling strength, respectively, while the averaged results also overestimate the buckling strength. In contrast, the results using the rotational spring boundary conditions provide much improved accuracy. In the case of Iso-TLS, the clamped boundary condition is appropriate due to the large number of beam members overlapping and thus stiffening the ends of trusses. However, for alternative load cases that trigger other critical buckling modes or TLS topologies with fewer overlapping trusses, this might not be true. Nevertheless, the rotation spring boundaries predict more accurate results than the average one and provide a sufficiently accurate estimation of the true buckling strength. Also, as expected, this spring model provides a lower bound for the true strength. This observation promises that the effective buckling strength of the whole lattice structure can be predicted by the buckling behavior of individual members.

Fig. 6 shows the impact of the boundary conditions on the buckling strength surfaces for arbitrary directional uni-axial loads provided by the simplified model. The rotated uni-axial loads are obtained by $\boldsymbol{\sigma}^0_{\text{rot}} = \boldsymbol{R}\boldsymbol{\sigma}^0_{\text{m}}\boldsymbol{R}^T$, where $\boldsymbol{\sigma}^0_{\text{m}}$ is the matrix-formated uni-axial load of $\boldsymbol{\sigma}^0 = [-1, 0, 0, 0, 0, 0]^T$ and $\boldsymbol{R}$ is a rotation matrix containing two Euler angles θ_1 and θ_2 that span over 0 to $\pi/2$ to cover the entire rotated stresses (see Fig. 6A) (Wang and Sigmund, 2020b). The surfaces are described by two Euler angles, and the associated buckling strength magnitudes describe the size. Consistent with the SC-PLS results from Fig. 5, the buckling strength estimated using simply-supported, rotational spring, averaged and clamped boundary conditions increases. Interestingly, the surfaces do not have the exact same shapes, which means that the effect of boundary conditions is not just a scaling of the strength. Specifically, it can be observed that when going from a coordinate axis to a near maximum strength angle, the path is flat for the simply-supported case (Fig. 6B), while it is curved for the clamped case (Fig. 6E), highlighting the non-linear contributions from the adjacent member stiffnesses.

In summary, the rotational spring boundary conditions yield sufficiently accurate estimations of the microstructural buckling strength with a significant improvement compared to the simply-supported, clamped boundary conditions and the corresponding average, when the uni-axial loading coincides with a principal axis. It is further shown that the simply-supported and clamped boundary conditions can be used as lower and upper bounds while the corresponding average results predict higher buckling strength than the one from the rotational spring boundary conditions.

3. Results and discussion

In this section, we employ the local member approach to investigate the performance of the lattice structures under rotated uni-axial loadings. Buckling strength is estimated using the local member approach subjected to the rotational spring boundary conditions and the average result under the simply-supported and clamped boundary conditions.

Fig. 7 shows the directional stiffness and strength surfaces of the SC-PLS, Iso-PLS, Iso-TLS, and an improved buckling strength isotropic configuration of the Iso-PLS, which will be discussed later. The two Euler angles that are used to describe the load direction are shown in Fig. 7A, where the principal axes in the Cartesian coordinate system are shown on all the lattices and surfaces.

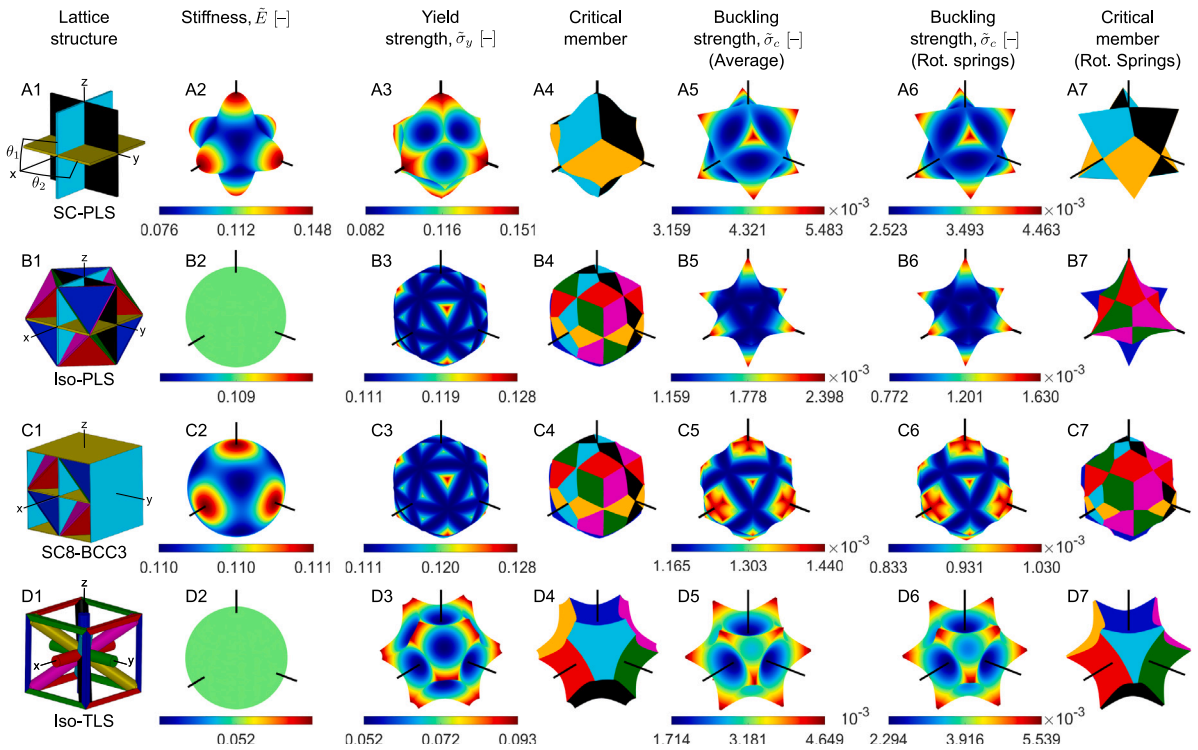

Fig. 7. Relative directional stiffness and strength surfaces of the lattice structures at volume fraction $f \approx 0.2$. A1, B1, C1, D1: Lattice topologies with colored plate or truss member sets and load orientation descriptions with two Euler angles. The front black plate is hidden for the SC8-BCC3. A2, B2, C2 and D2: Directional stiffness surfaces. A3, B3, C3 and D3: Directional yield strength surfaces. A4, B4, C4 and D4: Colored member set that fails due to yielding under given load directions. A5, B5, C5 and D5: Directional buckling strength surface estimated using the average values from simply-supported and clamped boundary conditions. A6, B6, C6 and D6: Directional buckling strength surface estimated using the rotational spring boundary conditions. A7, B7, C7 and D7: Colored member set that fails due to buckling under given load directions. All surfaces are depicted with Cartesian coordinate system axes.

3.1. Performance of SC-PLS, Iso-PLS and Iso-TLS

The SC-PLS exhibits strong anisotropy in both stiffness and strength. It has the highest and lowest directional stiffness when the load is aligned with two SC plates (i.e. is aligned with the normal axis of the third set of SC plates) and is furthest away from all the plates, respectively (Fig. 7A2). Correspondingly, the highest yield strength arises when the load is aligned with two SC plates (Fig. 7A3). Fig. 7A4 shows the critical plate, corresponding to the colored plates of Fig. 7A1, that has the lowest yield strength for a given angle. The high yield strength angles can intuitively be seen where the critical plate is at intersections of different plate sets (Fig. 7A4). For comparison, the lowest yield strength arises when the load is aligned with any single plate. In order to get a comparison of the strength anisotropy of the considered lattice structures, the yield strength anisotropy index is employed and defined as the ratio between the highest and the lowest strength, and this value for the SC-PLS is $\tilde{\sigma}_{y,max}/\tilde{\sigma}_{y,min} = 1.84$. The buckling strength surfaces from the two different local member evaluations possess a similar shape, and the same critical buckling member is predicted using these two approaches for a given load direction. Again, the average buckling strength is higher than the one from the rotational spring boundaries. The anisotropy indices of the buckling strength are $\tilde{\sigma}_{c,max}/\tilde{\sigma}_{c,min} = 1.73$ and 1.77, respectively. Furthermore, the highest buckling strength arises when the stresses are evenly distributed among all the plates (Fig. 7 A5 and A6)and the corresponding angles are located at intersections between critical plate sets (Fig. 7A7).

The Iso-PLS has isotropic stiffness, visualized by a perfect sphere (Fig. 7B2). Although isotropic stiffness does not necessarily result in isotropic strength, its yield strength surface is close to being isotropic (Fig. 7B3) with $\tilde{\sigma}_{y,max}/\tilde{\sigma}_{y,min} = 1.16$. The lowest and highest yield strengths appear when the load is aligned and furthest away from the plate sets, respectively. The highest yield strength angles are at the intersection points by three plate sets (Fig. 7B4). This excludes the intersection points where the load is aligned with any single plate, e.g. $\theta_1 = 0\,\text{deg}$ and $\theta_2 = 45\,\text{deg}$. In contrast to the nearly isotropic yield strength surface, the buckling strength surface is much more anisotropic (Fig. 7B5 and B6). This observation holds for both buckling strength surfaces. The corresponding strength anisotropy indices are 2.07 and 2.11. The highest buckling strength is obtained when the load is aligned with two SC plate sets (the black, yellow, or cyan plate sets). The associated critical plate visualization (Fig. 7B7) reveals that only the BCC plates are susceptible to buckling failure. The reason is that the BCC plates (the red, green, blue, and magenta plate sets) are significantly thinner than the SC plates. The highest buckling strength is located at the angle furthest away from the BCC plates, i.e., aligned with SC plates which also helps by carrying the majority of the stress. Correspondingly, the lowest buckling strength is when the load is aligned with any single BCC plate set.

The Iso-TLS also has isotropic stiffness (Fig. 7D2), but its yield strength surface is more anisotropic than the Iso-PLS (Fig. 7D3). This is because trusses only provide axial stiffness while plates offer planar stiffness. Its highest yield strength is also located at the load angle furthest away from any truss set directions, i.e., at the intersection of three different truss sets. (Fig. 7D4). The corresponding yield anisotropy index is $\tilde{\sigma}_{y,max}/\tilde{\sigma}_{y,min} = 1.79$. Furthermore, its buckling strength surface (Fig. 7D5 and D6) resembles the yield strength surface, with $\tilde{\sigma}_{c,max}/\tilde{\sigma}_{c,min} = 2.71$ for the average and $\tilde{\sigma}_{c,max}/\tilde{\sigma}_{c,min} = 2.41$ for rotational springs. The critical truss surface (Fig. 7D7) has a similar shape as the critical yield truss surface. Different from PLSs, the rotational spring boundary condition predicts higher buckling strength than the average, which is consistent with the uni-axial evaluation in Fig. 5C.

3.2. Isotropic Iso-PLS configuration with improved buckling strength isotropy

Based on the knowledge gained from the local member approach and the critical member plots, the isotropy of the buckling strength surface of Iso-PLS can be improved by providing the same number of adjacent members for all the BCC plates. Specifically, this can be achieved by splitting single SC plates into two parts by keeping one half of the thickness in the middle and distributing the other half to the outer faces of the unit cell, which creates a boundary box (see Fig. 7C1, where the front black plate is hidden). Following the naming convention from Tancogne-Dejean and Mohr (2018), where the Iso-PLS is an SC-BCC3 PLS, the new configuration is an SC8-BCC3 PLS. This new configuration only consists of the theoretically more isotropic tetrahedral holes, whereas the Iso-PLS has extra octahedral holes when tessellated through space (e.g., the closest blue plate in Fig. 7B1). This new configuration stiffens all the BCC plates equally, while insignificantly changing the stiffness or yield strength surfaces, as almost the same amount of volume is retained in all directions. By simply splitting the SC plates in two parallel plates, there is a change in the amount of overlapping volume, which leads to a tiny deterioration in isotropy, as seen in Fig. 7 C2. In order to recover perfect stiffness isotropy, the thickness ratio between the SC and BCC plates needs to be slightly adjusted (just as it has been done for the original Iso-PLS). The shapes of the yield strength and critical member surfaces of the new lattice structure stay the same as for the Iso-PLS (Fig. 7C3 and C4). In contrast, its buckling strength surface (Fig. 7C5 and C6) is more isotropic and resembles the yield strength surface. The lowest and highest strengths remain at the same directions as above, but the buckling strength anisotropy index is now reduced to $\tilde{\sigma}_{c,max}/\tilde{\sigma}_{c,min} = 1.24$ for both evaluations. Note that recovering perfect stiffness isotropy would decrease and increase the thicknesses of SC and BCC plates, respectively, resulting in a lower buckling strength anisotropy index. Lastly, the resemblance of the yield and buckling strength surfaces can also be seen by studying the critical plates (Fig. 7C7).

3.3. Summary

Isotropic stiffness does not necessarily result in isotropic strength. Nevertheless, Iso-TLS and SC8-BCC3 have yield strength surfaces that resemble their buckling strength surfaces. In contrast, SC-PLS and Iso-PLS have vastly different strength surfaces. Similar and more isotropic strength surfaces result in more predictable failure mechanisms based on the volume fractions and the base material, whereas dissimilar surfaces also depend on load orientations. In general, the highest yield and buckling strength of the lattice structures arise when the stresses are equally distributed between the members, for instance when the load is furthest away from the members or when a majority of members are aligned with the load direction. Furthermore, low slenderness of a member also provides high buckling strength. Interestingly, Iso-PLS has higher stiffness and yield strength for all load directions than Iso-TLS, but conversely, Iso-TLS has higher buckling strength for all load directions.

3.4. Verification of buckling strength surfaces

The buckling strength surfaces from the local member approach are further verified by investigating two load angles of interest per lattice structure, besides the load aligned with a principal axis (Fig. 5). Only these two extremal points are investigated due to the very high CPU cost associated with the "exact" analysis using Floquet–Bloch for non-axially loaded microstructures. These two points are selected as extreme points of the failure surfaces and are thus expected to provide upper bounds on the errors of the local member approach. The comparisons between the local member approach subjected to the different boundary conditions and the accurate linear microstructural buckling analysis presented in Section 2.1 are shown in Table 2. The relative error is calculated with respect to the accurate buckling strength calculation, where a positive or negative value implies underestimation or overestimation, respectively.

For the SC-PLS, the investigated angles are the minimum strength angle where the load is aligned with only one SC plate and the maximum strength angle where the load is furthest away from all plates. The investigated angles for Iso-PLS and SC8-BCC3 are the minimum strength angle where the load is aligned with only the green BCC plate set and the high strength angle where the load is perpendicular to the blue BCC plate sets. The investigated angles for the Iso-TLS are the high strength angle where the load is aligned with the cyan BCC truss and the maximum strength angle where the load is furthest away from all trusses. In most cases, the rotational spring model underestimates the buckling strength except for the maximum strength angle for Iso-TLS, where the rotational spring model overestimates the buckling strength by −26.78%. Here, the overestimation is caused by the fact that the critical buckling mode is not cell periodic. The comparisons among evaluations from the local member model with different boundary conditions confirm the previous observations, where (1) the simply-supported and clamped models provide lower and upper bounds on buckling strength, respectively; (2) the average model predicts higher buckling strength for PLSs and lower buckling strength for Iso-TLS than the rotational spring model; (3) The rotational spring model underestimates buckling strength, and (4) the average model may under- or over-estimate the buckling strength, even if the buckling mode is local cell-periodic.

We remark that the rotational spring boundary condition has much larger errors in all the considered angles for the SC8-BBC3 than the average value of the simply-supported and clamped boundary conditions. The big errors are partly from the simplification of the effective length, which is especially pronounced for the isotropic lattice structures as they have non-perpendicular overlapping members and the shortening effects are larger. Furthermore, the inter-connectivity between the stiffeners of the PLSs is not considered, which again is especially pronounced for the isotropic PLSs as they have many overlapping members. Finally, the neglect of pre-stress in the adjacent members further enlarges the estimation errors. Hence, the average model provides better predictions in this case.

Despite obvious errors, the rotational spring boundary condition provides an overall more reliable lower bound than simpler boundary conditions. On the other hand, it is infeasible to create microstructural buckling strength surfaces using accurate linear microstructural buckling analyses. For example, the investigated lattice structures (Fig. 1) need at least a crude sweep over $9 \cdot 9 \cdot 9$ wavevectors $k_j \in [-\pi, \pi]$ when subjected to complex load cases where the Brillouin zone cannot be reduced to the boundaries of a polyhedron. The average computational time using 24 CPU's is approximately 100 hours in COMSOL per load case per lattice (Andersen et al., 2020). In contrast, the computational time of the local member approach is approximately 5 seconds per member set. Hence, the local member approach, including the rotational spring boundary condition and the average value of the simply-supported and clamped boundary conditions, supported by some unit cell analysis sanity checks, is a viable solution to investigate the strengths and weaknesses of lattice structures.

4. Conclusions

We employ local member analyses to predict the strength of stretch-dominated TLSs and PLSs, which yields good accuracy compared to extremely costly microstructural FE-based buckling analysis. Comparison between different evaluations and accurate buckling evaluations shows that (1) As expected, simply-support and clamped boundary conditions provide lower and upper bounds; (2) Their averaged values predict higher buckling strength for PLSs and lower for Iso-TLS than the rotational spring model; (3) The rational spring boundary condition underestimates buckling strength while the average model may under-

Table 2
Comparison of buckling estimates for the accurate linear microstructural buckling analysis. Two angles of interest per lattice are compared to verify the local member approach with the addition of the load oriented along principal axes from Fig. 5.

Lattice structure	θ_1 deg	θ_2 deg	Floquet–Bloch	Simply supported (error %)	Average (error %)	Rotational springs (error %)	Clamped (error %)
SC-PLS	0	0	3.36E-3	2.22E-3 (33.84)	3.94E-3 (−17.26)	2.94E-3 (12.51)	5.66E-3 (−68.37)
	0	45	3.39E-3	2.00E-3 (41.10)	3.16E-3 (6.78)	2.52E-3 (25.56)	4.32E-3 (−27.52)
	35.26	45	5.12E-3	3.59E-3 (29.96)	5.49E-3 (−7.13)	4.47E-3 (12.86)	7.38E-3 (−44.10)
Iso-PLS	0	0	1.91E-3	1.37E-3 (28.22)	2.40E-3 (−25.39)	1.63E-3 (14.66)	3.42E-3 (−79.30)
	24.09	26.57	1.32E-3	6.43E-4 (51.27)	1.16E-3 (12.39	7.72E-4 (41.50)	1.67E-3\ (−26.85)
	35.26	45	1.40E-3	7.83E-4 (44.09)	1.40E-3 (−0.11)	9.38E-4 (32.99)	2.02E-3 (−44.41)
SC8-BCC3	0	0	1.53E-3	7.84E-4 (48.58)	1.43E-3 (6.73)	1.03E-3 (32.78)	2.07E-3 (−35.77)
	24.09	26.57	1.36E-3	6.47E-4 (52.57)	1.16E-3 (14.45)	8.33E-4 (38.91)	1.68E-3 (−23.47)
	35.26	45	1.55E-3	7.87E-4 (49.36)	1.41E-3 (9.13)	1.01E-3 (34.95)	2.03E-3 (−30.72)
Iso-TLS	0	0	2.59E-3	7.56E-4 (70.83)	1.72E-3 (33.67)	2.30E-3 (11.34)	2.68E-3 (−3.30)
	0	45	4.37E-3	2.28E-3 (47.92)	4.86E-3 (−11.10)	5.54E-3 (−26.78)	7.43E-3 (−69.93)
	35.26	45	3.54E-3	1.32E-3 (62.74)	2.81E-3 (20.62)	3.21E-3 (9.30)	4.30E-3 (−21.57)

or over-estimate buckling strength. In general, errors are found to be larger for non-member aligned loading, where bending effects are expected to be higher.

The local member approach is used to study directional buckling strength surfaces of the considered lattice structures. The findings reveal that isotropic stiffness does not necessarily result in isotropic (both yield and buckling) strength and that yield and buckling strength surfaces can also be widely different. It is by now known that PLSs have higher stiffness and yield strength, while TLSs have higher buckling strength, at least in the low volume fraction limit. However, we further show that the PLSs can have vastly different directional buckling strength surfaces than their yield strength surfaces. For specific base material and volume fraction combinations, buckling or yielding could dominate the critical failure mode depending on the load directions. In contrast, (isotropic) TLSs have similar buckling and yield strength surfaces, resulting in more predictable failure modes that are mainly based on the base material and volume fractions. We further create a new isotropic plate lattice configuration to improve the buckling strength isotropy using the knowledge gained in the buckling strength surface evaluation. Furthermore, the yield and buckling strength surfaces are also very similar for this configuration.

Future studies include investigation of the sensitivity and determination of the worst-case scenario of lattices subjected to arbitrary loads following an approach such as Wang et al. (2019). Furthermore, it is also interesting to investigate how the local member models compare to results from finite lattice studies (Wang and Sigmund, 2020a; Bluhm et al., 2022; Wang et al., 2022) and specifically when utilized as infill in macrostructures (Clausen et al., 2016). Finally, the local member analyses pave the way for efficiently accounting for local buckling failure in multiscale topology optimization (Groen et al., 2020).

Declaration of competing interest

The authors declare that they have no known competing financial interests or personal relationships that could have appeared to influence the work reported in this paper.

Acknowledgment

We acknowledge the financial support from the Villum Foundation through the Villum Investigator Project InnoTop.

References

Andersen, M.N., Wang, F., Sigmund, O., 2020. On the competition for ultimately stiff and strong architected materials. Mater. Des. 109356.
Bensoussan, A., Lions, J.-L., Papanicolaou, G., 2011. Asymptotic Analysis for Periodic Structures, Vol. 374. American Mathematical Soc.
Berger, J., Wadley, H., McMeeking, R., 2017. Mechanical metamaterials at the theoretical limit of isotropic elastic stiffness. Nature 543, 533–537.
Bluhm, G.L., Christensen, K., Poulios, K., Sigmund, O., Wang, F., 2022. Experimental verification of optimized hierarchical materials with superior buckling strength. (in review).
Bordiga, G., Cabras, L., Piccolroaz, A., Bigoni, D., 2021. Dynamics of prestressed elastic lattices: Homogenization, instabilities, and strain localization. J. Mech. Phys. Solids 146, 104198.
Bourdin, B., Kohn, R.V., 2008. Optimization of structural topology in the high-porosity regime. J. Mech. Phys. Solids 56, 1043–1064.
Christensen, R., 1986. Mechanics of low density materials. J. Mech. Phys. Solids 34, 563–578.
Clausen, A., Aage, N., Sigmund, O., 2016. Exploiting additive manufacturing infill in topology optimization for improved buckling load. Engineering 2, 250–257.
Deshpande, V.S., Fleck, N.A., Ashby, M.F., 2001. Effective properties of the octet-truss lattice material. J. Mech. Phys. Solids 49, 1747–1769.
Gibson, L.J., Ashby, M.F., Echajer, G.S., Robertson, C.I., 1982. The mechanics of two-dimensional cellular materials.. Proc. R. Soc. Lond. Ser. A Math. Phys. Eng. Sci. 382, 25–42.
Groen, J.P., Stutz, F.C., Aage, N., Bærentzen, J.A., Sigmund, O., 2020. De-homogenization of optimal multi-scale 3d topologies. Comput. Methods Appl. Mech. Engrg. 364, 112979.
Guedes, J., Kikuchi, N., 1990. Preprocessing and postprocessing for materials based on the homogenization method with adaptive finite element methods. Comput. Methods Appl. Mech. Engrg. 83, 143–198.
Gurtner, G., Durand, M., 2014. Stiffest elastic networks. Proc. R. Soc. A 470, 20130611.
Haghpanah, B., Papadopoulos, J., Mousanezhad, D., Nayeb-Hashemi, H., Vaziri, A., 2014. Buckling of regular, chiral and hierarchical honeycombs under a general macroscopic stress state. Proc. R. Soc. A 470, 20130856.
Latture, R.M., Begley, M.R., Zok, F.W., 2018. Design and mechanical properties of elastically isotropic trusses. J. Mater. Res. 33, 249–263.

Lopez-Pamies, O., Castañeda, P.P., 2007a. Homogenization-based constitutive models for porous elastomers and implications for macroscopic instabilities: I—analysis. J. Mech. Phys. Solids 55, 1677–1701.
Lopez-Pamies, O., Castañeda, P.P., 2007b. Homogenization-based constitutive models for porous elastomers and implications for macroscopic instabilities: Ii—results. J. Mech. Phys. Solids 55, 1702–1728.
Michel, J.-C., Lopez-Pamies, O., Castañeda, P.P., Triantafyllidis, N., 2007. Microscopic and macroscopic instabilities in finitely strained porous elastomers. J. Mech. Phys. Solids 55, 900–938.
Neves, M.M., Sigmund, O., Bendsœ, M.P., 2002. Topology optimization of periodic microstructures with a penalization of highly localized buckling modes. Internat. J. Numer. Methods Engrg. 54, 809–834.
Papka, S.D., Kyriakides, S., 1994. In-plane compressive response and crushing of honeycomb. J. Mech. Phys. Solids 42, 1499–1532.
Papka, S., Kyriakides, S., 1999. Biaxial crushing of honeycombs:—part 1: Experiments. Int. J. Solids Struct. 36, 4367–4396.
Sigmund, O., 1994. Materials with prescribed constitutive parameters: an inverse homogenization problem. Int. J. Solids Struct. 31, 2313–2329.
Tancogne-Dejean, T., Diamantopoulou, M., Gorji, M., Bonatti, C., Mohr, D., 2018. 3D plate-lattices: an emerging class of low-density metamaterial exhibiting optimal isotropic stiffness. Adv. Mater. 30, 1803334.
Tancogne-Dejean, T., Mohr, D., 2018. Elastically-isotropic truss lattice materials of reduced plastic anisotropy. Int. J. Solids Struct. 138, 24–39.
Thomsen, C.R., Wang, F., Sigmund, O., 2018. Buckling strength topology optimization of 2D periodic materials based on linearized bifurcation analysis. Comput. Methods Appl. Mech. Engrg. 339, 115–136.
Triantafyllidis, N., Nestorović, M., Schraad, M., 2006. Failure surfaces for finitely strained two-phase periodic solids under general in-plane loading. J. Appl. Mech. 73, 505–515.
Triantafyllidis, N., Schnaidt, W.C., 1993. Comparison of microscopic and macroscopic instabilities in a class of two-dimensional periodic composites. J. Mech. Phys. Solids 41, 1533–1565.
Triantafyllidis, N., Schraad, M., 1998. Onset of failure in aluminum honeycombs under general in-plane loading. J. Mech. Phys. Solids 46, 1089–1124.
Valdevit, L., Godfrey, S.W., Schaedler, T.A., Jacobsen, A.J., Carter, W.B., 2013. Compressive strength of hollow microlattices: Experimental characterization, modeling, and optimal design. J. Mater. Res. 28, 2461–2473.
Wang, F., Brøns, M., Sigmund, O., 2022. Architected materials with extreme stiffness and strength. (in preparation).
Wang, Y., Groen, J.P., Sigmund, O., 2019. Simple optimal lattice structures for arbitrary loadings. Extreme Mech. Lett. 29, 100447.
Wang, F., Sigmund, O., 2020a. Numerical investigation of stiffness and buckling response of simple and optimized infill structures. Struct. Multidiscip. Optim. 1–11.
Wang, Y., Sigmund, O., 2020b. Quasiperiodic mechanical metamaterials with extreme isotropic stiffness. Extreme Mech. Lett. 34, 100596.
Wang, F., Sigmund, O., 2021. 3D architected isotropic materials with tunable stiffness and buckling strength. J. Mech. Phys. Solids 152, 104415.